The contributions of the actin machinery to endocytic membrane bending and vesicle formation

Andrea Picco[a,†], Wanda Kukulski[b,c,d,†,*], Hetty E. Manenschijn[a,b], Tanja Specht[b], John A. G. Briggs[b,d,e], and Marko Kaksonen[a,*]

[a]Department of Biochemistry and NCCR Chemical Biology, University of Geneva, 1211 Geneva, Switzerland; [b]Cell Biology and Biophysics Unit and [d]Structural and Computational Biology Unit, European Molecular Biology Laboratory, 69117 Heidelberg, Germany; [c]Cell Biology Division and [e]Structural Studies Division, MRC Laboratory of Molecular Biology, Cambridge CB2 0QH, United Kingdom

ABSTRACT Branched and cross-linked actin networks mediate cellular processes that move and shape membranes. To understand how actin contributes during the different stages of endocytic membrane reshaping, we analyzed deletion mutants of yeast actin network components using a hybrid imaging approach that combines live imaging with correlative microscopy. We could thus temporally dissect the effects of different actin network perturbations, revealing distinct stages of actin-based membrane reshaping. Our data show that initiation of membrane bending requires the actin network to be physically linked to the plasma membrane and to be optimally cross-linked. Once initiated, the membrane invagination process is driven by nucleation and polymerization of new actin filaments, independent of the degree of cross-linking and unaffected by a surplus of actin network components. A key transition occurs 2 s before scission, when the filament nucleation rate drops. From that time point on, invagination growth and vesicle scission are driven by an expansion of the actin network without a proportional increase of net actin amounts. The expansion is sensitive to the amount of filamentous actin and its cross-linking. Our results suggest that the mechanism by which actin reshapes the membrane changes during the progress of endocytosis, possibly adapting to varying force requirements.

INTRODUCTION

Arp2/3-mediated actin filament networks play key roles in generating and controlling force for movement and reshaping of cellular membranes (Rotty et al., 2013). These cytoskeletal assemblies drive diverse processes such as cell motility at the leading edge, formation of lamellipodia, and generation of actin comet-tails for the intracellular movement of endosomes and pathogens (Taunton et al., 2000; Pollard and Borisy, 2003; Welch and Way, 2013), as well as several endocytic uptake pathways including clathrin-mediated endocytosis (Pelkmans et al., 2002; Galletta, Mooren, and Cooper, 2010; Collins et al., 2011; Boulant, Kural, et al., 2011). These fundamental cellular functions rely on force generation by treadmilling of actin monomers through a dendritic actin network built from a set of conserved protein components. The network architecture and dynamics are modulated through its composition (Svitkina, 2013). Thus, actin network properties can adjust to meet the requirements of different processes. However, it remains poorly understood how variations in network properties control the mechanisms of force generation in cells and how the force requirements vary during actin-driven processes.

Endocytosis in budding and fission yeasts is strictly dependent on Arp2/3-based actin polymerization (Kubler and Riezman, 1993; Moreau, Galan, et al., 1997; Kaksonen, Sun, and Drubin, 2003;

Abbreviations used: CLEM, correlative light and electron microscopy; CP, cytoplasm; CW, cell wall; EM, electron microscopy; GFP, green fluorescent protein; HPF, high-pressure freezing; NPF, nucleation-promoting factor; PM, plasma membrane; SC, synthetic complete.

Galletta and Cooper, 2009), which provides force that drives membrane invagination against membrane tension and against the turgor pressure inside yeast cells (Aghamohammadzadeh and Ayscough, 2009; Basu *et al.*, 2014). The process generally conforms to the dendritic nucleation model (Berro *et al.*, 2010; Sirotkin *et al.*, 2010). The membrane is coupled to actin through endocytic adaptors at the tip of the invagination, while nucleation and filament elongation occur at the plasma membrane (Kaksonen, Sun, and Drubin, 2003; Idrissi *et al.*, 2012; Skruzny *et al.*, 2012; Chen and Pollard, 2013; Berro and Pollard, 2014; Picco *et al.*, 2015). Most molecular constituents of the yeast endocytic actin network have homologues in mammalian Arp2/3-mediated actin networks (Boettner *et al.*, 2011a).

In this study, we aimed at understanding mechanistically how the endocytic actin network contributes throughout the process of membrane deformation and vesicle formation in the budding yeast *Saccharomyces cerevisiae*. We therefore deleted genes that encode proteins involved in coupling actin to the membrane, actin filament cross-linking, or regulation of actin nucleation. We studied these mutants using a hybrid imaging approach, which makes use of correlative microscopy data and of live cell imaging and particle tracking data (Kukulski *et al.*, 2011; 2012a; Kukulski, Picco, *et al.*, 2016; Picco *et al.*, 2015; Picco and Kaksonen, 2017). This approach provides measurements of membrane morphology and actin network volume as well as high-resolution information on protein localization and assembly dynamics. We could thus observe and quantify very subtle phenotypes caused by specific actin network perturbations. Our previously published wild-type data sets served us as reference data for interpreting the results presented here (Kukulski *et al.*, 2012a; Picco *et al.*, 2015). Our findings reveal three subsequent stages in the actin network lifetime, suggesting that different actin-based mechanisms may function during endocytic membrane shaping.

RESULTS

Initiation of membrane bending requires actin-membrane coupling via clathrin adaptor proteins

The molecular mechanisms that cause the initial bending of the endocytic membrane in vivo are unknown. While our previous data indicated that initiation of membrane invagination coincides with the assembly of actin, and inhibiting actin polymerization with latrunculin A prevents membrane bending at endocytic sites (Kukulski *et al.*, 2012a; Picco *et al.*, 2015), immunoelectron microscopy data suggested that curvature of the endocytic membrane is induced before actin network assembly (Idrissi *et al.*, 2012). Indeed, endocytic adaptor proteins could modulate membrane curvature before actin assembly through their membrane-binding domains or through crowding, as demonstrated in vitro (Boucrot, Pick, Camdere, *et al.*, 2012; Stachowiak, Schmid, *et al.*, 2012; Busch *et al.*, 2015; Skruzny, Desfosses, *et al.*, 2015). Epsins and Sla2 (the yeast homologue of Hip1R), act cooperatively to couple the membrane to the actin network via their membrane- and actin-binding domains, and are essential for endocytic vesicle formation (Kaksonen, Sun, and Drubin, 2003; Sun *et al.*, 2005; Boettner *et al.*, 2011b; Skruzny *et al.*, 2012). We deleted the actin-binding domains of both Sla2 and Ent1 (*sla2ΔTHATCH ent1ΔACB-GFP*) to test whether the presence of the membrane binding-domains of these endocytic adaptor proteins is sufficient for initiating membrane bending when actin is assembling, but the transmission of the force from the actin cytoskeleton is uncoupled from the plasma membrane (Skruzny *et al.*, 2012). Fluorescence time-course imaging showed that cells carrying these mutations fail to form endocytic vesicles and coat proteins remain immobile during actin polymerization (Skruzny *et al.*, 2012). However, it remained

unclear whether the membrane is bent at these arrested endocytic sites. By applying correlative light microscopy and electron tomography to these cells, we targeted 12 sites marked by the colocalization of GFP-labeled epsin and Abp1-mCherry as a marker for the presence of an actin network. In all the target localizations, we found no invaginations but only flat plasma membranes associated with large cytoplasmic zones excluding ribosomes (Figure 1A). The ribosome exclusion zones correlate with the extent of the endocytic machinery, including the actin network (Kukulski *et al.*, 2012a). In a similar experiment on cells in which the whole *SLA2* gene was deleted, all 11 target localizations of Sla1-GFP and Abp1-mCherry also showed flat plasma membranes associated with large exclusion zones (Figure 1B; Table 1). In wild-type cells, ~1% of the endocytic events have a flat membrane in the presence of the actin network, while the remaining 99% show either a membrane invagination or a vesicle (Kukulski *et al.*, 2012a). Our results suggest that actin polymerization and the presence of the membrane-binding coat proteins are not sufficient to induce stable membrane curvature if they are not coupled to each other. The coupling of the membrane to a polymerizing actin network via the actin-binding domains of Sla2 and Ent1 is thus necessary to facilitate or stabilize the initiation of the endocytic membrane invagination (Figure 1C).

Actin filament cross-linking is critical for the initiation of membrane bending and for reaching scission stage

The composition of actin networks modulates their mechanical properties. For instance, the stiffness of actin gels decreases with a lower density of actin filament cross-linkers (Blanchoin *et al.*, 2014). In yeasts, the actin cross-linking activity of fimbrin has been shown to be essential for endocytic internalization (Kubler and Riezman, 1993; Kaksonen, Toret, and Drubin, 2005; Skau *et al.*, 2011). We perturbed actin filament cross-linking by deleting the yeast fimbrin Sac6 and studied *sac6Δ* cells by live imaging and correlative microscopy to investigate the effects on membrane invagination and vesicle formation.

We first tracked the dynamic behavior of the coat protein Sla1-GFP in *sac6Δ* cells by live imaging with high spatiotemporal resolution (Picco and Kaksonen, 2017). Sla1 is positioned close to the invagination tip and can be used to track the movement of the membrane invagination and the vesicle into the cell (Idrissi *et al.*, 2008; Picco *et al.*, 2015; Kukulski, Picco, *et al.*, 2016). In *sac6Δ* cells, we found three distinct types of Sla1-GFP behavior (Figure 2A). The majority of Sla1 spots (78.4 ± 5.5%, mean ± SE, 145 endocytic events in nine cells; Figure 2A; see *Materials and Methods* and Table 2) remained immobile at the plasma membrane until they disassembled, consistent with earlier studies (Kaksonen, Toret, and Drubin, 2005; Gheorghe *et al.*, 2008). However, 15.1 ± 4.4% (mean ± SE, 145 endocytic events in nine cells) of events revealed distinctive behavior: The initial phase of centroid movement was very similar to that in wild-type cells, but ~90 nm away from the plasma membrane, the centroid started to retract toward the plasma membrane (Figure 2, A and B). The remaining 6.5 ± 2.2% (mean ± SE, 145 endocytic events in nine cells) of Sla1-GFP spots were motile and moved inward, similarly to the Sla1-GFP wild-type cells (Figure 2, A and C).

To visualize the membrane morphology directly, we applied correlative microscopy to *sac6Δ* cells expressing Sla1-GFP and Abp1-mCherry. In wild-type cells, the presence of these proteins marks events that span from initiation of membrane bending until disassembly of the actin network from the newly formed endocytic vesicle (Kukulski *et al.*, 2012a). In *sac6Δ*, we found that, in the presence of both Abp1 and Sla1, as well as in the presence of Abp1 only, the
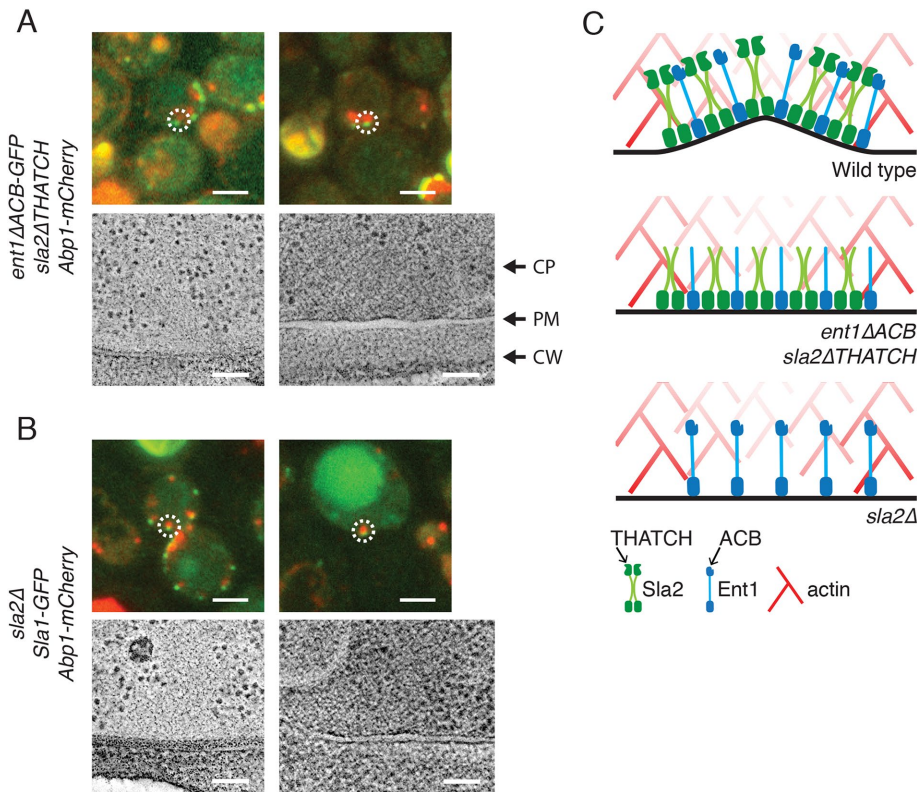
FIGURE 1: Correlative microscopy of endocytosis in cells with the actin cytoskeleton uncoupled from the plasma membrane. (A) Top row shows overlaid red and green channel fluorescence images of resin sections of yeast cells expressing *ent1ΔACB-GFP*, *sla2ΔTHATCH*, and Abp1-mCherry. Endocytic sites targeted by correlative microscopy are marked by white dashed circles. Bottom row shows virtual slices from electron tomograms at the corresponding locations. (B) Top row shows overlaid red and green channel fluorescence images of resin sections of *sla2Δ* yeast cells expressing Sla1-GFP and Abp1-mCherry. Endocytic sites targeted by correlative microscopy are marked by white dashed circles. Bottom row shows virtual slices from electron tomograms at the corresponding locations. In both A and B, the panels to the left show examples of the flattest membranes in each data set. The panels on the right show examples of the most bent membranes in each data set. The data set sizes were *n* = 12 (A), *n* = 11 (B). All panels are oriented so that the cytoplasm (CP) is above the plasma membrane (PM), and the cell wall (CW) is below. Scale bars are 2 μm in fluorescence images, 100 nm in electron tomography images. (C) Model representation for the assembly of Sla2, Ent1, and the actin cytoskeleton. In wild-type cells, assembly of intact Sla2, Ent1, and actin leads to bending of the membrane. In the absence of the actin-binding domains of Sla2 and Ent1, THATCH and ACB, respectively, or in the absence of full-length Sla2, the membrane remains flat despite actin polymerization.

majority of endocytic sites were flat membranes (72 and 62%, *n* = 25 and 34, respectively) and the remaining ones were invaginations (28 and 38%, *n* = 25 and 34, respectively) (Figure 3, A and B). We did not find endocytic vesicles at any of the sites, confirming that successful scission events are very rare in *sac6Δ* cells. These data also support the live cell–imaging observation that the majority of the Sla1-GFP spots remained immobile throughout their lifetimes. The immobile spots are thus likely to indicate events in which membrane bending is not initiated, despite assembly of the actin network.

We then measured the lengths of the invaginations marked by the presence of Abp1-mCherry and Sla1-GFP, or by the presence of Abp1-mCherry and absence of Sla1-GFP, in *sac6Δ* cells. We found that all the invaginations were less than 100 nm long, while in wild-type cells invaginations are up to 140 nm long (Kukulski *et al.*, 2012a; Figure 3C). These measurements are in agreement with the live imaging finding that most invaginations retract before reaching 100 nm in length (Figure 2B).

We also measured the curvature of invagination tips in *sac6Δ* cells. As in wild-type cells, the tips reached a minimum radius for invaginations of ~40 nm. However, the average tip radius for invaginations longer than 40 nm was significantly greater in *sac6Δ* cells than in wild-type cells (*sac6Δ*: 15.5 nm, SD 3.7 nm, *n* = 12; wild type: 11.6 nm, SD 2.6 nm, *n* = 47; *p* = 0.0003; Supplemental Figure S1). Thus, either wider tips are a property of all invaginations in *sac6Δ* cells, or widening of invagination tips occurs during retraction, possibly due to disassembly of coat proteins.

Taken together, our results indicate that in the absence of the actin cross-linker Sac6,

Yeast strain	Data set size: number of endocytic structures obtained from CLEM data	Number of individual fluorescent signals analyzed by CLEM	Number of tomograms acquired to obtain the data set	Number of EM grids imaged by CLEM to obtain the data set	Number of HPF samples (yeast pellets in resin block) used to obtain the data set
sla2Δ, Sla1-EGFP, Abp1-mCherry	11	11	5	2	1
ent1ΔACB-GFP, sla2ΔTHATCH, Abp1-mCherry	12	12	9	2	1
sac6Δ, Sla1-EGFP, Abp1-mCherry	60	59	41	6	1
bbc1Δ, Sla1-EGFP, Abp1-mCherry	58	52	35	3	2[a]
bbc1Δ, Rvs167-EGFP, Abp1-mCherry	37	29	21	2	1

[a]From two different cell cultures.

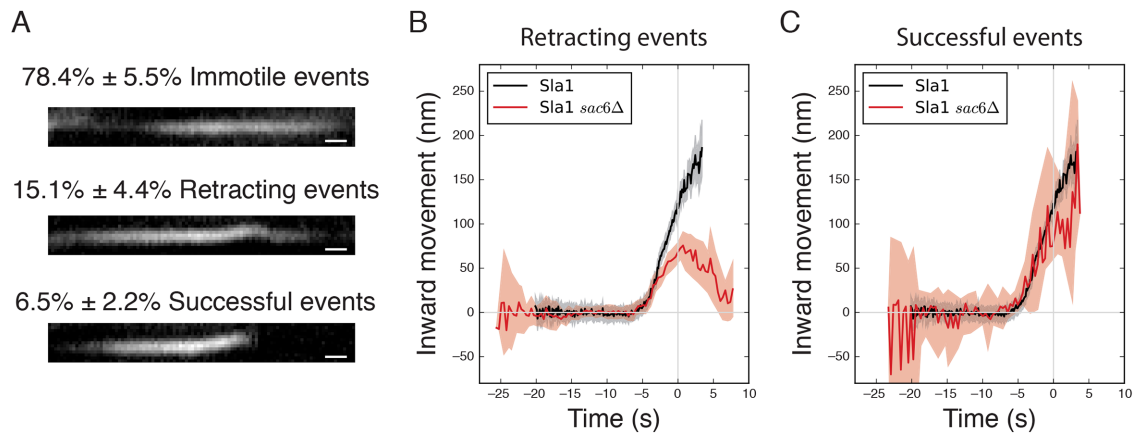**TABLE 1:** Sample sizes of correlative microscopy data.

FIGURE 2: Live imaging of endocytosis in cells with impaired actin cross-linking. (A) Representative kymographs of the three distinct behaviors of Sla1-GFP spots in *sac6Δ* cells and the percentage of occurrence for each type of event (mean ± SE, *n*= 9 cells). Scale bars correspond to 5 s. (B) The inward movement of Sla1-GFP average trajectories of retracting events in *sac6Δ* cells (red) and in wild-type cells (black; Picco *et al.*, 2015). (C) The inward movement of Sla1-GFP average trajectories of successful events in *sac6Δ* cells (red) and in wild-type cells (black; Picco *et al.*, 2015). The shadows in B and C correspond to the 95% confidence interval. Time 0 in B and C marks the scission event (Kukulski *et al.*, 2012a; Picco *et al.*, 2015).

endocytosis is blocked either at the stage of initial membrane bending, or at an invagination length of ~100 nm, followed by a retraction of the invagination. Remarkably, in events that initiate membrane bending, elongation of the invagination appears to be unaffected until retraction occurs. In rare cases, endocytosis progresses further and likely leads to successful vesicle formation.

Perturbed actin nucleation in *bbc1Δ* cells enhances propulsion of vesicles

Arp2/3-dependent nucleation of actin filaments is driven by nucleation-promoting factors (NPFs) at cellular membranes (Pollard, 2007; Campellone and Welch, 2010). The NPF Las17, a yeast N-WASP orthologue, is required for actin assembly at endocytic sites,

and its activity is negatively regulated by Bbc1 in vitro (Rodal *et al.*, 2003; Sun, Martin, and Drubin, 2006). At endocytic sites, Bbc1 colocalizes with actin spots (Kaksonen, Toret, and Drubin, 2005). We perturbed the rate of actin filament nucleation by deleting *BBC1*. In *bbc1Δ* cells, endocytic actin spots are brighter and the endocytic coat moves inward faster and over a longer distance than in wild-type cells (Kaksonen, Toret, and Drubin, 2005).

To understand how actin nucleation in the absence of Bbc1 affects invagination dynamics, we first tracked Sla1-GFP dynamics in *bbc1Δ* cells. The average centroid trajectory of Sla1-GFP in *bbc1Δ* cells showed an initial movement at the same speed as in wild-type cells. About 7 s later, approximately when scission occurs in wild-type cells, Sla1 centroid movement accelerated and it moved

	Protein	Number of single-color trajectories used to generate the average trajectory	Number of cells imaged to obtain the single-color trajectories	Number of trajectory pairs used for spatial and temporal alignment	Number of cells imaged to obtain the trajectory pairs
bbc1Δ	Abp1	52	13	NA	NA
bbc1Δ	Rvs167	65	14	56	21
bbc1Δ	Sla1	49	13	47	13
bbc1Δ	Arc18	51	15	61	20
bbc1Δ	Las17	NA	NA	50	19
sac6Δ	Sla1 motile	7	15	NA	NA
sac6Δ	Sla1 retracting	19	15	NA	NA
Wild type	Abp1	66	13	NA	NA
Wild type	Rvs167	60	13	262	69
Wild type	Sla1	67	13	58	14
Wild type	Arc18	70	14	90	12
Wild type	Las17	NA	NA	49	15

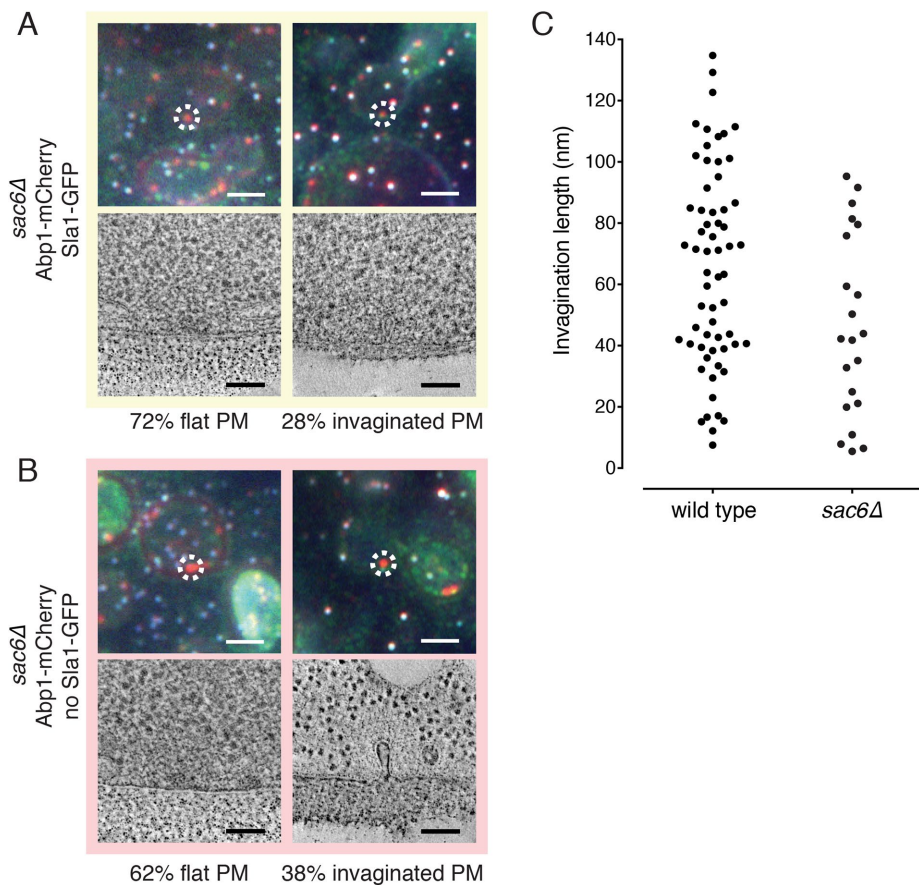**TABLE 2:** Sample sizes of live imaging data.

FIGURE 3: Correlative microscopy of endocytosis in cells with impaired actin cross-linking. (A) Top row shows overlaid red, green, and blue channel fluorescence images of resin sections through *sac6Δ* yeast cells expressing Abp1-mCherry and Sla1-GFP. The blue channel indicates TetraSpeck fiducial markers for correlation. White dashed circles mark endocytic sites where Abp1-mCherry and Sla1-GFP colocalize, targeted by correlative microscopy. Bottom row is virtual slices from electron tomograms at the corresponding localizations. Of *n* = 25 sites, 72% displayed flat plasma membranes and 28% showed invaginations. (B) Top row shows overlaid red, green, and blue channel fluorescence images of resin sections through yeast cells. The blue channel indicates TetraSpeck fiducial markers for correlation. White dashed circles mark endocytic sites where Abp1-mCherry is present but Sla1-GFP is absent, targeted by correlative microscopy. Bottom row shows virtual slices from electron tomograms at the corresponding localizations. Of *n* = 34 sites, 62% displayed flat plasma membranes and 38% showed invaginations. Scale bars are 2 µm in fluorescence images, 100 nm in electron tomography images. (C) The distribution of endocytic invagination lengths measured in the electron tomograms of *sac6Δ* cells. The wild-type data (Kukulski *et al.*, 2012a) are shown for comparison.

We then imaged Abp1-GFP, which we used as a marker for the dynamics of the endocytic actin network (Kaksonen, Sun, and Drubin, 2003). In wild-type cells, the recruitment of Abp1 coincides with the start of the Sla1 inward movement, which marks membrane invagination (Picco *et al.*, 2015). In *bbc1Δ* cells, the recruitment of Abp1 preceded the start of Sla1-GFP inward movement by ~4 s, indicating that actin assembly does not immediately lead to membrane bending. The centroid of Abp1-GFP initially localized closer to the plasma membrane than in wild-type cells (Figure 4C), suggesting a different distribution of the actin filaments on the membrane. Interestingly, the Sla1 inward movement began when the Abp1-GFP centroid reached the same height as in wild-type cells.

The endocytic actin spots are brighter in *bbc1Δ* cells (Kaksonen, Toret, and Drubin, 2005). We therefore measured the number of Abp1-GFP and Arc18-GFP molecules present at endocytic sites over time (Joglekar *et al.*, 2006; Lawrimore *et al.*, 2011; Picco *et al.*, 2015; Figure 4D; Supplemental Figure S2B; see *Materials and Methods*). Abp1 and Arc18 were recruited to the endocytic sites at the same rate as in wild-type cells (Picco *et al.*, 2015). However, because assembly of the actin network in *bbc1Δ* cells lasted for ~5 s longer than in wild-type cells, the fully assembled network contained more Abp1 and Arc18 molecules. At the time when scission occurred, the number of Abp1 molecules recruited to the endocytic site was about doubled (Figure 4D), while the number of Arc18 was ~25% larger than in wild type (Supplemental Figure S2B).

The Abp1-GFP centroid in *bbc1Δ* cells began moving inward at the same speed as in wild-type cells. However, the speed of the Abp1 centroid drastically increased when the invagination length reached

100 nm, ~2 s before scission (Figure 4C). Interestingly, while the Abp1 centroid accelerated, the assembly rate of Abp1 molecules remained unchanged and then dropped (Figure 4D).

We next performed correlative microscopy of *bbc1Δ* cells expressing Sla1-GFP and Abp1-mCherry, as well as *bbc1Δ* cells expressing Rvs167-GFP and Abp1-mCherry. Similarly to wild-type cells, we found endocytic invaginations and vesicles in the presence of Abp1 and Sla1 or Rvs167, as well as in the presence of Abp1 but the absence of Sla1 or Rvs167 (Figure 5, A and B). We measured that endocytic vesicles were positioned up to 600 nm from the plasma membrane, which is significantly farther away from the plasma membrane than in wild-type cells (*bbc1Δ*: 288.7 nm, SD: 158.7 nm, *n* = 47; wild type: 129.5 nm, SD: 39.7 nm, *n* = 62; *p* < 0.0001; Figure 5C). This result is in striking agreement with the enhanced movement of Sla1-GFP and Rvs167-GFP, starting around scission. Taken together, these results suggest that vesicles are

deeper into the cell than in the wild type (Figure 4A). We next investigated the dynamics of the amphiphysin Rvs167 in *bbc1Δ* cells. In wild-type cells, the peak of Rvs167-GFP fluorescence intensity marks the scission event and coincides with a fast inward movement of the Rvs167-GFP centroid (Picco *et al.*, 2015). In *bbc1Δ* cells, Rvs167-GFP showed a pronounced movement into the cytoplasm, which was concomitant with its peak in number of molecules (Figure 4B; Supplemental Figure S2A), in 85 ± 6% (median ± SE, 195 endocytic events in 14 cells) of the endocytic events. Like Sla1-GFP, motile Rvs167-GFP spots also moved deeper into the cell cytoplasm (Figure 4B). In the remaining 15 ± 6% (median ± SE, 195 endocytic events in 14 cells) of events, Rvs167-GFP spots appeared immotile. The trajectories of Sla1-GFP and Rvs167-GFP indicate that *bbc1Δ* does not significantly affect the rate of invagination growth. However, they suggest that, after scission, vesicles move deeper into *bbc1Δ* cells than into wild-type cells.

being propelled faster and deeper into the cytoplasm upon deletion of Bbc1.

To better resolve the effects of $bbc1\Delta$ on vesicle formation, we measured the surface areas of endocytic vesicles and compared them to the wild type. We found that vesicles in $bbc1\Delta$ cells were on average 25% larger ($bbc1\Delta$: 7998 nm^2, SD: 2838 nm^2, $n = 47$; wild type: 6380 nm^2, SD: 1929 nm^2, $n = 62$; $p = 0.0004$; Figure 5D). The larger vesicle sizes indicate either that scission occurred when invaginations were longer, or that scission sites on the invaginations were positioned closer to the plasma membrane than in wild-type cells. The putative sites of scission are the necks of invaginations, which we found to be positioned similarly to those in wild-type cells (Supplemental Figure S2C). However, we found that there were longer invaginations in $bbc1\Delta$ cells than in the wild type (Supplemental Figure S2D), suggesting that the inward movement of the membrane, observed through centroid tracking of Sla1-GFP (Figure 4A), might accelerate shortly before scission, leading to longer invaginations that result in larger vesicles.

Actin assembly occurs on a larger membrane area in $bbc1\Delta$ cells

To detail whether the increase in Abp1 molecules is accompanied by an increase in actin network size in $bbc1\Delta$ cells, we measured the dimensions of the ribosome exclusion zones surrounding invaginations. We found that the volumes of exclusion zones in $bbc1\Delta$ cells were significantly larger than those in wild-type cells ($bbc1\Delta$: 0.0052 fl, SD = 0.0029 fl, $n = 21$; wild type: 0.0028 fl, SD = 0.0017 fl, $n = 62$; $p = 0.0001$), which was in line with the increased numbers of Abp1-GFP molecules that we measured by fluorescence microscopy. Interestingly, while the heights of the exclusion zones in $bbc1\Delta$ correlated with the invagination lengths as observed in wild-type cells (Figure 5E; Kukulski et al., 2012a), the exclusion zone diameters were independent of the stage of the invagination process and significantly larger than in wild-type cells (Figure 5F; $bbc1\Delta$: mean = 235.1 nm, SD = 48.2 nm, $n = 21$; wild type: mean = 181.2 nm, SD = 40.9 nm, $n = 62$; $p < 0.0001$). Note that to compute the above values, we only considered exclusion zones of $bbc1\Delta$ invaginations below 135 nm in length, so that the invagination lengths compared with those of the wild-type population. The enlarged diameters of the exclusion zones indicate that the actin cytoskeleton is distributed over a larger surface area of the plasma membrane when nucleation of actin is initiated. Therefore, despite the height of the actin network being comparable to that in the wild type during the invagination process, the volume of the actin network is higher.

As in wild-type cells, vesicles in $bbc1\Delta$ cells were surrounded by ribosome exclusion zones that were either connected or disconnected to the plasma membrane (Figure 5, A and B). We previously
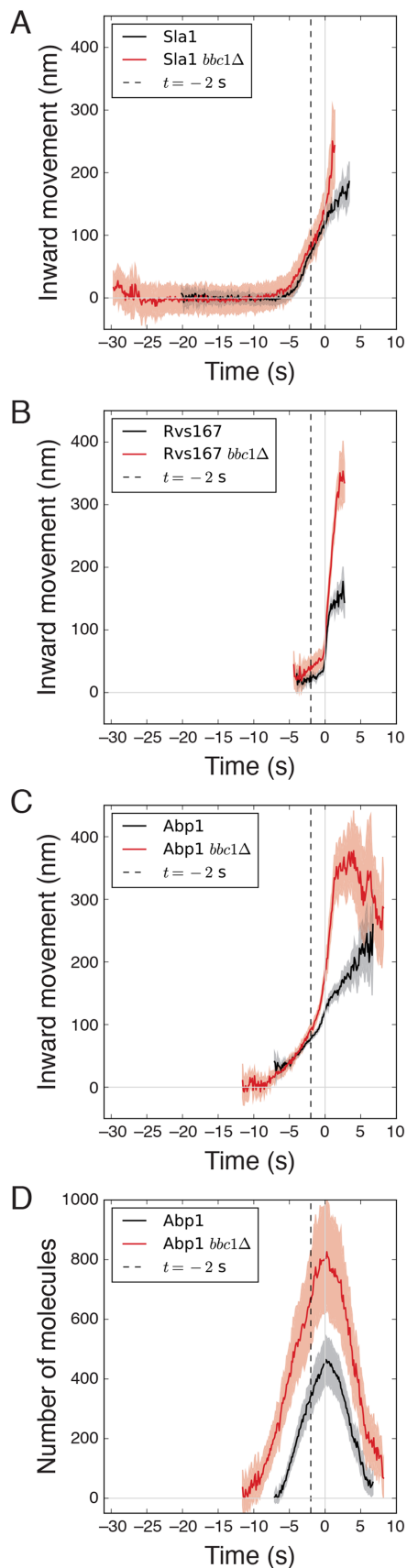
FIGURE 4: Live imaging of endocytosis in cells with perturbed actin nucleation. (A) The inward movement of Sla1-GFP average trajectories in $bbc1\Delta$ (red) and in wild-type (black) cells. (B) The inward movement of Rvs167-GFP average trajectories in $bbc1\Delta$ (red) and in wild-type (black) cells. (C) The inward movement of Abp1-GFP average trajectories in $bbc1\Delta$ (red) and in wild-type (black) cells. (D) The number of Abp1-GFP molecules over time in $bbc1\Delta$ (red) and in wild-type (black) cells. The shadows in A–D correspond to the 95% confidence interval. The trajectories in $bbc1\Delta$ and wild-type cells were independently aligned in space and in time to Abp1 (Picco and Kaksonen, 2017). The 0 on the Y-axis marks the position of Sla1-GFP before the invagination movement starts. The 0 on the X-axis marks the scission event (see *Image analysis and trajectory alignment*; Kukulski et al., 2012a; Picco et al., 2015; Picco and Kaksonen, 2017). The wild-type trajectories are from Picco et al. (2015).
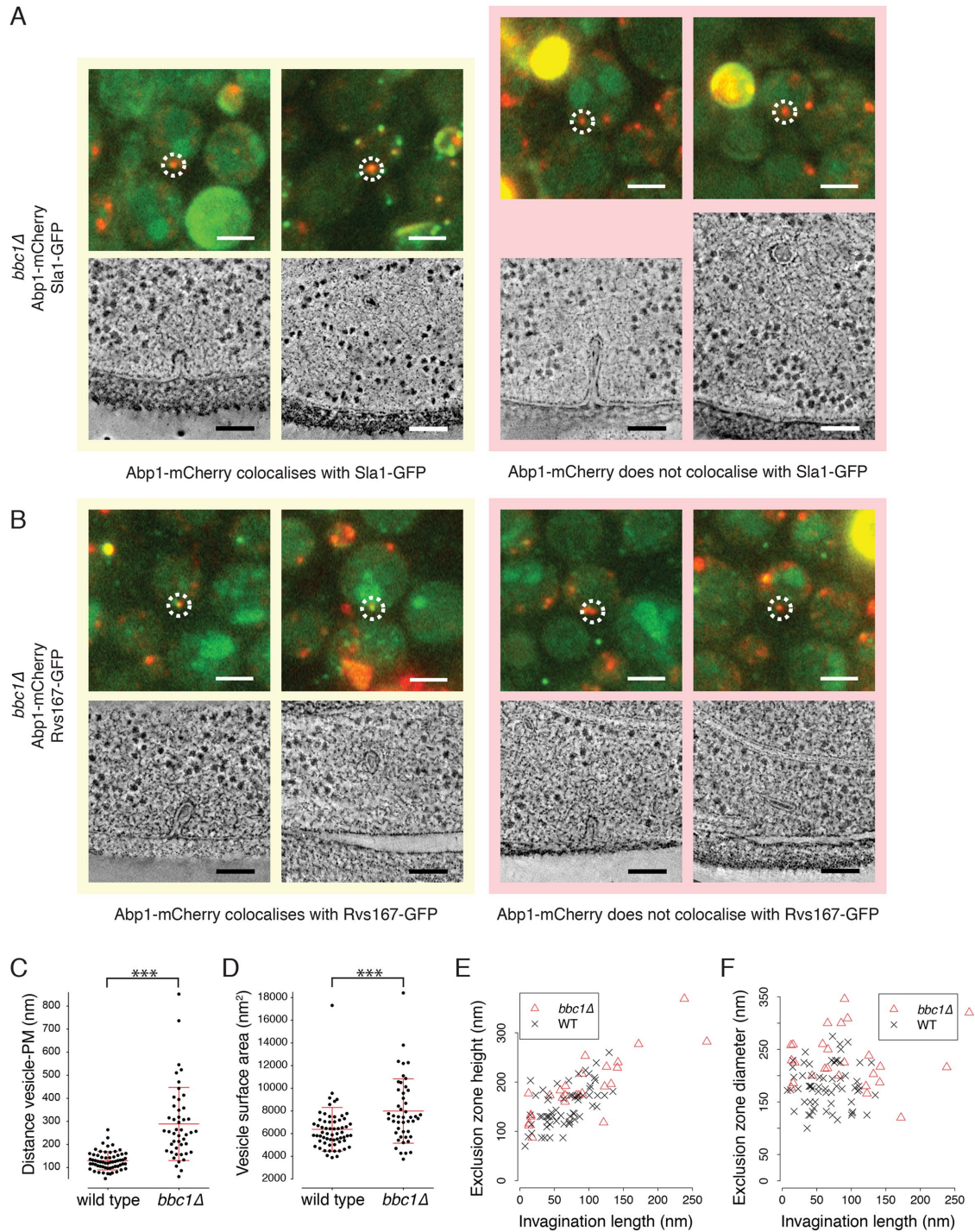
FIGURE 5: Correlative microscopy of endocytosis in cells with perturbed actin nucleation. (A) *bbc1Δ* cells expressing Abp1-mCherry and Sla1-GFP. Top row shows overlaid red and green channel fluorescence images of resin sections through yeast cells. White dashed circles mark endocytic sites where Abp1-mCherry and Sla1-GFP colocalize (yellow box) or where Abp1-mCherry is present but Sla1-GFP is absent (pink box), targeted by correlative microscopy. Bottom row is virtual slices from electron tomograms at the corresponding localizations. (B) *bbc1Δ* cells expressing Abp1-mCherry and Rvs167-GFP. Top row shows overlaid red and green channel fluorescence images of resin sections through yeast cells. White dashed circles mark endocytic sites where Abp1-mCherry and Rvs167-GFP colocalize (yellow box), or where Abp1-mCherry is present but Rvs167-GFP is absent (pink box), targeted by correlative microscopy. Bottom row is virtual slices from electron tomograms at the corresponding localizations. Scale bars are 2 μm in fluorescence images, 100 nm in electron tomography images. (C) The shortest distance between vesicle centers and the plasma membrane (PM) in wild-type and *bbc1Δ* cells. (D) The surface areas of vesicles in *bbc1Δ* cells. Red lines in C and D represent the mean and SD. $p < 0.0001$ in C, and $p = 0.0004$ in D. (E) The heights of exclusion zones surrounding invaginations plotted against invagination lengths. (F) The diameters of exclusion zones surrounding invaginations plotted against invagination lengths. Data from wild-type cells in C–F are from Kukulski *et al.* (2012a).

suggested that the first case represents the earliest phase of the vesicle lifetime (Kukulski *et al.*, 2012a). In *bbc1Δ* cells, only 20% of vesicles had exclusion zones connected to the plasma membrane, as compared with 70% in wild-type cells. Therefore, we conclude that the density of the actin network near the plasma membrane decreases earlier in *bbc1Δ* cells than in wild-type cells. This asymmetric change in density could shift the centroid of Abp1-GFP toward the cell center, contributing to enhancing the movement of the Abp1-GFP centroid in *bbc1Δ* cells.

Accumulation of Las17 drops before scission, while network expansion and movement continue in *bbc1Δ* cells

We next investigated the number of molecules of Las17 at the endocytic site. Las17 is a NPF and putative target of Bbc1 (Rodal *et al.*, 2003; Kaksonen, Toret, and Drubin, 2005). Las17 accumulates on the plasma membrane, where it activates the Arp2/3 complex to nucleate actin filament formation (Winter, Lechler, and Li, 1999; Sun, Martin, and Drubin, 2006). We found that in *bbc1Δ* cells, Las17 accumulated over a longer time than in wild-type cells (Figure 6). In wild-type cells, the rate at which Las17 molecules accumulate decreases after invagination growth begins. The number of Las17 molecules reaches a peak of ~45 molecules and then starts decreasing ~2 s before scission (Picco *et al.*, 2015). In *bbc1Δ*, however, the rate at which Las17 molecules accumulate remained high during membrane invagination, and the number of Las17 molecules continued to increase until it reached a peak of ~80 molecules, before decreasing ~2 s before scission as in wild-type cells (Figure 6). The assembly of the actin cytoskeleton in *bbc1Δ* cells began when ~40 Las17 molecules had accumulated, as in wild-type cells. Taken together, these data show that in *bbc1Δ* cells, Las17 accumulation is unhindered and the number of accumulating Las17 molecules is larger than in the wild type, suggesting that Bbc1 is negatively regulating the assembly of Las17. Further, the data suggest that Bbc1 is not required for triggering disassembly of Las17.
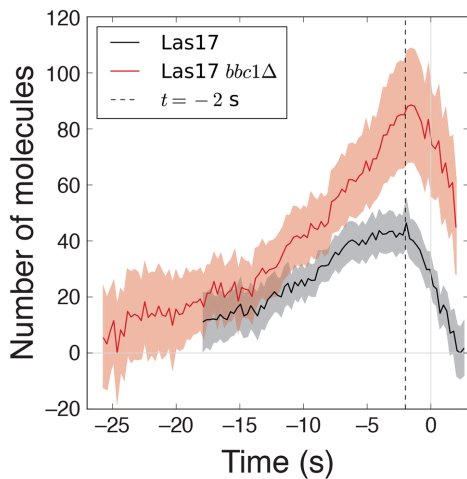
In summary, in *bbc1Δ* cells, the actin network starts accumulating on a larger membrane area than in wild-type cells, resulting in higher network volumes. Nevertheless, the velocity of the actin centroid movement and the height of the exclusion zones are similar to those in wild-type cells up to ~2 s before scission. In the last 2 s before scission occurs, when the accumulation of Las17 drops, the actin network centroid movement significantly speeds up. Thus, the rate and progression of the invagination process are unaffected in *bbc1Δ* cells until shortly before scission. The changes in actin network behavior seem to interfere only with the shape of late invaginations, which can become longer than in wild-type cells and therefore result in larger vesicles, and with the movement of vesicles, which are pushed farther into the cytoplasm.

DISCUSSION

The endocytic actin network is critical for invaginating the plasma membrane during endocytosis (Merrifield *et al.*, 2002; Kaksonen, Sun, and Drubin, 2003; Boulant, Kural, *et al.*, 2011; Kukulski *et al.*, 2012a). We genetically manipulated different biochemical activities related to assembly and connectivity of the actin network to gain understanding of the molecular mechanisms underlying endocytic membrane bending.

On the basis of the mutant phenotypes that we studied, we can define three sequential stages in the actin network lifetime (Figure 7). The first stage corresponds to assembly of the actin network until initiation of membrane bending occurs. The second stage spans the time of invagination growth up to ~100 nm, 2 s before vesicle scission. During the second stage, the numbers of Arp2/3 and actin molecules increase, suggesting that the growth of the invagination is driven by nucleation and polymerization of actin filaments (Berro *et al.*, 2010; Sirotkin *et al.*, 2010; Picco *et al.*, 2015). The third stage spans the last 2 s of the invagination and the formation of the endocytic vesicle. During the third stage, the numbers of Arp2/3 and Abp1 molecules reach their maxima and start to decrease. This may be because the numbers of the main NPFs, Las17 and Myo5, decrease, leading to a reduced rate of filament nucleation and polymerization (Picco *et al.*, 2015), or because there is an increase in actin filament severing and depolymerization (Chen and Pollard, 2013) while the polymerization rate remains unaltered, or a combination of both. Whatever the mechanism that controls the net amount of actin components is, the centroids of actin cytoskeletal proteins continue moving inward, and the actin network volume increases. These results indicate that the network expands although the number of actin components is not increasing proportionally. These observations support a model where different mechanisms of propulsion are used during the second and third stages (Idrissi *et al.*, 2012).

Endocytosis is critically dependent on the actin-binding regions of the clathrin adaptors Sla2 and Ent1 (Skruzny *et al.*, 2012). Here we show that their actin-binding regions are important for enabling the initiation of membrane bending in yeast cells. Clathrin adaptor proteins can bend membranes in vitro (Boucrot, Pick, Camdere, *et al.*, 2012; Stachowiak, Schmid, *et al.*, 2012; Busch *et al.*, 2015; Skruzny, Desfosses, *et al.*, 2015) but our results suggest that in yeast cells the assembly of the clathrin adaptors, when disconnected from the network of actin filaments, is not sufficient to stably initiate membrane bending (Figure 7). Our data do not rule out the occurrence of transient membrane bending, which may have been too unstable or rare to be captured. Indeed, shallow membrane invaginations have been observed at endocytic sites in *sla2Δ* cells (Idrissi *et al.*, 2012). However, these results were obtained under different

FIGURE 6: Live imaging of nucleation-promoting factor in cells with perturbed actin nucleation. The number of Las17-GFP molecules is shown over time in *bbc1Δ* (red) and in wild-type (black) cells. The shadows correspond to the 95% confidence interval. Time 0 marks the scission event, which is timed according to the peak in the Rvs167 number of molecules, when aligned in time to Abp1 (see *Image analysis and trajectory alignment*; Kukulski *et al.*, 2012a; Picco *et al.*, 2015). The wild-type data are from Picco *et al.* (2015).
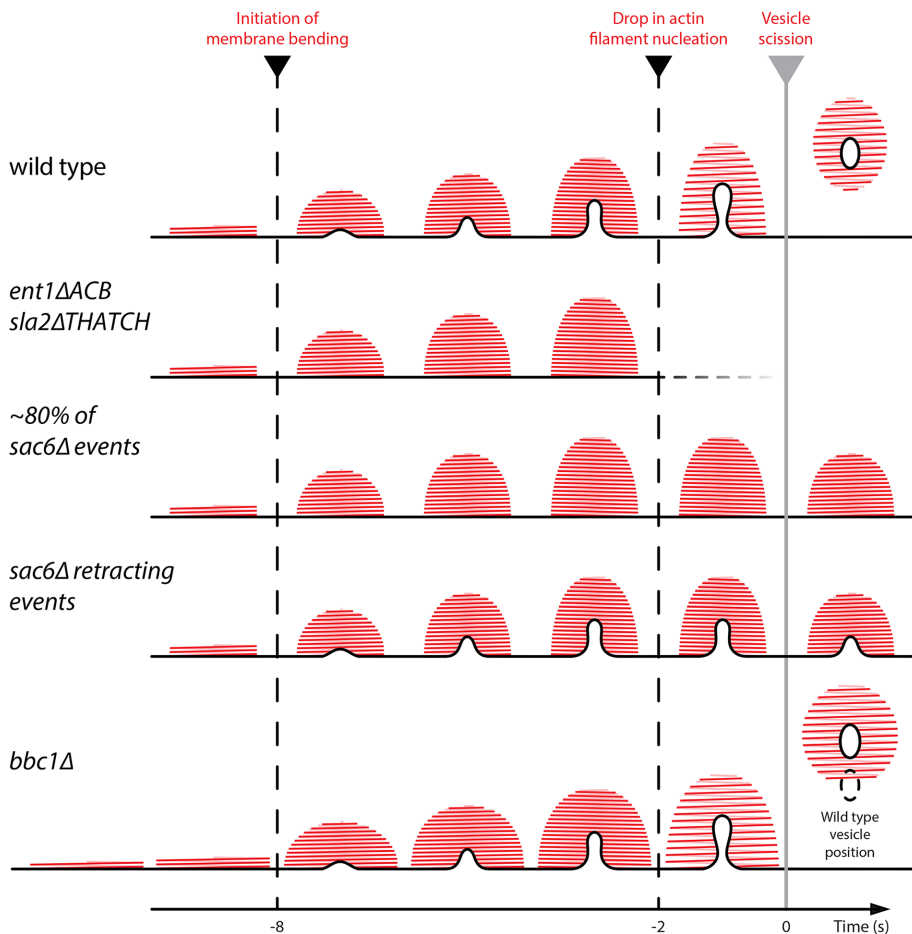
FIGURE 7: The actin network pulls the plasma membrane invagination in three distinct stages, which correspond to 1) actin network assembly until the initiation of membrane bending is achieved, 2) invagination growth driven by actin nucleation and polymerization, and 3) expansion of the actin network after the nucleation of new actin filaments has dropped 2 s before scission. The transitions between the stages are indicated by the dashed lines. *ent1ΔACB, sla2ΔTHATCH* prevents initiation of membrane bending. Likewise, *sac6Δ* hinders initiation of membrane bending in the majority of cases. If membrane bending is initiated, the plasma membrane invagination proceeds until 2 s before scission and then retracts. In rare cases, invagination growth proceeds further through scission of the vesicle, as in wild-type cells. *bbc1Δ* allows the plasma membrane to invaginate normally, but the actin network is larger and expands ~2 s before scission. In *bbc1Δ* the vesicle is propelled deeper into the cytoplasm than in wild-type cells.

experimental conditions, which may have lowered the turgor pressure inside the yeast cells and shifted a possible equilibrium between flat membranes and transient curvature toward the latter (Idrissi and Geli, 2014).

In *sac6Δ* cells, most of the endocytic events fail to initiate the invagination process. Sac6-mediated cross-linking of actin filaments is thus important for initial bending of the plasma membrane. In about one-fifth of the events, membrane bending is initiated and the invaginations grow normally up to ~100 nm in length, which in wild-type cells corresponds to ~2 s before scission (Picco *et al.*, 2015). The second stage is thus unaffected in *sac6Δ* cells if membrane bending is initiated. However, the majority of invaginations in *sac6Δ* cells retract and only very few events proceed through apparently normal scission of the vesicle. Therefore, cross-linking is likely to be important also for the expansion of the actin network, possibly by storing energy that could be released during the third stage that drives invagination growth through scission (Ma and Berro, 2017).

Interestingly, in fission yeast the number of cross-linkers per filament peaks just around the time of scission, suggesting that cross-linking might have a role in the later stage of plasma membrane invagination growth (Berro and Pollard, 2014). In the rare successful events in *sac6Δ* cells, stochastic variations in the process, for example, variations in the amount of other cross-linkers such as Scp1 (Aghamohammadzadeh and Ayscough, 2009), may allow the invagination to proceed through scission despite the absence of Sac6.

In *bbc1Δ* cells, more actin is assembled, which results in a wider actin network than in wild-type cells. The start of membrane bending in *bbc1Δ* cells is delayed with respect to the initiation of actin assembly, suggesting that during the first stage, the actin network is not organized in an optimal way to produce force for invagination growth. However, as soon as membrane bending is initiated, the invaginations in *bbc1Δ* cells grow at the same rate as in wild-type cells. During the third stage in *bbc1Δ* cells, the centroid movement of both actin cytoskeletal proteins and coat proteins is enhanced. This suggests that either a final expansion or a rearrangement of the actin network is strongly enhanced, probably because more actin is present, thereby accelerating the coat movement.

The force that is needed to pull a membrane tube depends on membrane shape and degree of protein coating (Derenyi *et al.*, 2002; Powers *et al.*, 2002; Koster *et al.*, 2005; Dmitrieff and Nedelec, 2015). For endocytosis, it has been suggested that the force required for the initiation of membrane bending is greater than the force needed to subsequently shape the membrane into a tubular invagination (Dmitrieff and Nedelec, 2015). On the basis of our observations, we speculate that the formation of the actin network might have evolved to allow force generation to adjust to the changing force requirements during the different stages of endocytosis. The cross-linking of actin filaments controls the mechanical properties of the actin network: a network of cross-linked actin filaments sustains larger stresses without deformation and has a higher elastic modulus than actin filaments alone (Sato *et al.*, 1987; Wachsstock *et al.*, 1994; Gardel *et al.*, 2004; Berro and Pollard, 2014; Bieling, Li, *et al.*, 2016). Optimal cross-linking of the actin filaments may thus be critical to initiate membrane bending when the force required is the highest. Once membrane bending is initiated, the force required for pulling an invagination likely decreases, and filament nucleation and actin polymerization are therefore sufficient to drive invagination growth in the absence of the cross-linker Sac6. However, when the nucleation of new filaments decreases during the last stage, the mechanical properties of the actin network become again important to provide the force necessary to proceed to the scission of the vesicle: a cross-linked actin network might be able to store and then release the

stress accumulated during the first part of the invagination growth, and thus expand and pull the invagination until scission occurs. The release of stress could occur either due to the elasticity of the whole actin network or as a consequence of cross-linker turnover, which could release filament contacts that were induced under higher loads. The enlarged actin network in *bbc1Δ* may accumulate more force than in wild-type cells, which could explain the speed-up during the final stage of endocytosis.

MATERIALS AND METHODS
Strain generation
Yeast strains were generated by homologous recombination of the target genes with PCR cassettes encoding for fluorescent tags (Janke *et al.*, 2004). The C-terminal fluorescent tags were inserted from plasmids pFA6a-EGFP-His3MX6, pFA6a-mCherry-KanMX4, and pYM12-PKS134, which was used for monomeric GFP (myEGFP).

Strains used for correlative light and electron microscopy.

sla2Δ, Sla1-EGFP, Abp1-mCherry (Skruzny *et al.*, 2012; MKY1195):

MATa, his3Δ200, leu2-3,112, ura3-52, lys2-801, sla2:natNT2, SLA1-EGFP::HIS3MX6, ABP1-mCherry::kanMX4

ent1ΔACB-EGFP, sla2ΔTHATCH, Abp1-mCherry (Skruzny *et al.*, 2012; MKY1846):

MATa/α, his3Δ200, ura3-52, lys2-801, ent1ΔACB(Δ amino acids 294–450)-EGFP::HIS3MX6, sla2ΔTHATCH::natNT2, ABP1-mCherry::kanMX4

sac6Δ, Sla1-EGFP, Abp1-mCherry (MKY2869):

MATa, his3Δ200, leu2-3,112, ura3-52, lys2-801, sac6:natNT2, SLA1-EGFP::HIS3MX6, ABP1-mCherry::kanMX4

bbc1Δ, Sla1-EGFP, Abp1-mCherry (MKY1805):

MATa, his3Δ200, leu2-3,112, ura3-52, lys2-801, bbc1::cgLEU2, SLA1-EGFP::HIS3MX6, ABP1-mCherry::kanMX4

bbc1Δ, Rvs167-EGFP, Abp1-mCherry (MKY1803):

MATa, his3Δ200, leu2-3,112, ura3-52, lys2-801, bbc1::cgLEU2, RVS167-EGFP::HIS3MX6, ABP1-mCherry::kanMX4

Strains used for fluorescence live microscopy.

bbc1Δ, Sla1-EGFP (MKY3412):

MATα, his3200, leu2-3,112, ura3-52, lys2-801, Sla1-EGFP::HIS3MX6, bbc1delta::natNT2

bbc1Δ, Abp1-EGFP (MKY3247):

MATa, his3200, leu2-3,112, ura3-52, lys2-801, Abp1-EGFP::HIS3MX6, bbc1delta::natNT2

bbc1, Rvs167-EGFP (MKY3416):

MATα, his3200, leu2-3,112, ura3-52, lys2-801, Rvs167-EGFP::HIS3MX6, bbc1delta::natNT2

bbc1Δ, Arc18-myEGFP (MKY3016):

MATa, his3200, leu2-3,112, ura3-52, lys2-801, Arc18-myEGFP::NAT, bbc1Δ::natNT2

bbc1Δ, Las17-EGFP (MKY3418):

MATa, his3200, leu2-3,112, ura3-52, lys2-801, Las17-EGFP::HISMX6, bbc1Δ::natNT2

bbc1Δ, Sla1-EGFP, Abp1-mCherry (MKY2059):

MATa, his3200, leu2-3,112, ura3-52, lys2-801, Sla1-EGFP::HIS3MX6, Abp1-mCherry::KANMX4, bbc1delta::cgLEU2

bbc1Δ, Abp1-mCherry, Rvs167-EGFP (MKY2061):

MATa, his3200, leu2-3,112, ura3-52, lys2-801, Rvs167-EGFP::HIS3MX6, Abp1-mCherry, bbc1delta::cgLEU2

bbc1Δ, Arc18-myEGFP, Abp1-mCherry (MKY3015):

MATα, his3200, leu2-3,112, ura3-52, lys2-801, Arc18-myEGFP::NAT, Abp1-mCherry::KANMX bbc1Δ::natNT2

bbc1Δ, Las17-EGFP, Abp1-mCherry (MKY2103):

MATα, his3200, leu2-3,112, ura3-52, lys2-801, Las17-EGFP::HIS3MX6, Abp1-mCherry::KANMX, bbc1delta::cgLEU2

Live cell imaging
Yeast strains were imaged as described before (Picco *et al.*, 2015; Picco and Kaksonen, 2017). Yeast cells were grown overnight at 25°C in SC-Trp. They were diluted in the morning and grown to log phase at 25°C. Cells were adhered to 25 mm coverslips (Menzel-Gläser #1), which were coated with Concanavalin A (100 µg/ml). Adhered cells were imaged in SC-Trp medium with an Olympus IX81 microscope and an Olympus 100×/1.45 NA TIRF objective. Cells were excited for 80–250 ms per exposure with a 488-nm laser or simultaneously with 488- and 561-nm lasers. For GFP-only images the emission light was filtered using a GFP-3035C-OMF single-band filter set (Semrock). For GFP and mCherry two-color simultaneous imaging, the excitation light was reflected with an OBS-U-M2TIR 488/561 (Semrock) dichroic mirror and the emission light was split and filtered with a DUAL-view beam splitter (Optical Insights).

Image analysis and trajectory alignment
Images were background-subtracted and corrected for photobleaching. Before the endocytic events were tracked, the cytoplasmic fluorescent signal was removed as described (Picco *et al.*, 2015; Picco and Kaksonen, 2017). Briefly, a median filter of radius 6 pixels was used to estimate the cytoplasmic fluorescent signal, which was then subtracted from the image itself. The endocytic events were tracked using the Particle Tracker plugin in Fiji/ImageJ (Sbalzarini and Koumoutsakos, 2005). Two-color trajectory positions were corrected for chromatic aberrations by applying a warping transformation that was computed from TetraSpeck bead images acquired under the same imaging conditions (Picco *et al.*, 2015). After that, the trajectories of each protein, with the exception of Las17-GFP, were aligned in space and in time and averaged using the trajalign module distribution available at http://apicco.github.io/trajectory_alignment/ (Picco and Kaksonen, 2017). Sla1-GFP average trajectories in Figure 2, B and C, were then aligned in time manually to compare their invagination dynamics. To align the average trajectories of each protein with those of the other proteins in the same yeast strain, we imaged simultaneously each protein of interest, tagged with EGFP, and Abp1, tagged with mCherry, in both wild-type and *bbc1Δ* strains. We then tracked the dynamics and the appearance of the proteins of interest with respect to Abp1 and we used these trajectories to register the position and appearance of each average trajectory with respect to Abp1 (Picco *et al.*, 2015; Picco and Kaksonen, 2017). As Las17-GFP does not move (Picco *et al.*, 2015), Las17 trajectories were tracked simultaneously with Abp1-mCherry trajectories. They were then aligned and averaged using the software in Picco *et al.* (2015), which used the spatial and temporal alignment that aligned the Abp1-mCherry trajectories together to compute the transformations that aligned Las17-GFP trajectories. The average trajectories in the different strains were then plotted together in Figures 4 and 6 using the

peak of the Rvs167 number of molecules in both the wild-type and *bbc1Δ* to mark time 0. In Figure 4, the positions along the *Y*-axis are the positions of the average trajectories with respect to Abp1 shifted so that the average centroid positions of Sla1 trajectories before the invagination dynamics start are centered on 0.

Quantification of the number of proteins

The average protein amounts were estimated by comparing the fluorescence intensities of the endocytic spots of the proteins of interest with the fluorescence intensity of Nuf2-GFP spots in cells imaged during their anaphase–telophase (Joglekar *et al.*, 2006; Picco *et al.*, 2015). The average amount of Arc18-myGFP was estimated by comparison to Nuf2-GFP spot intensities and by applying a correction constant of 0.68 ± 0.14 (Picco *et al.*, 2015). The average protein amounts were then used to calibrate the fluorescence intensity curves by scaling the average fluorescence intensity value (Picco *et al.*, 2015).

Correlative light and electron microscopy

Correlative light and electron microscopy was carried out as described before (Kukulski *et al.*, 2011, 2012b). Yeast cultures were grown at 25°C in SC-Trp medium to exponential phase. Cells were pelleted using vacuum filtration and high-pressure frozen using a Bal-tec HPM010 (McDonald, 2007). Freeze substitution, Lowicryl HM20 embedding, and sectioning were done according to the protocol in Kukulski *et al.* (2012a). As fiducial markers for the correlation procedure, we used either blue 20 nm FluoSpheres (Molecular Probes; Kukulski *et al.*, 2012a) or 50 nm TetraSpeck beads (Life Technologies; Suresh *et al.*, 2015). Fluorescence microscopy of the resin sections on electron microscopy grids was performed immediately after sectioning, as detailed in Kukulski *et al.* (2012b) and Suresh *et al.* (2015). Low-magnification (pixel size 2.53 nm) and high-magnification (pixel size 1.18 nm) electron-tomographic tilt series were acquired on a FEI Tecnai F30 microscope, set up as described (Kukulski *et al.*, 2012a) using Serial EM (Mastronarde, 2005), and reconstructed with IMOD (Kremer *et al.*, 1996). Centroids of GFP and mCherry signals were correlated with virtual slices of the low-magnification electron tomograms based on the fluorescent fiducial markers and in a second step with virtual slices of the high-magnification tomograms based on gold fiducial markers using MATLAB-based correlation procedures described in Kukulski *et al.* (2011).

Quantification of membrane shape parameters and ribosome exclusion zones

To quantify shapes of invaginations and vesicles as well as of ribosome exclusion zones, we used precisely the same procedures as for the wild-type data set (Kukulski *et al.*, 2012a). This allowed us to compare the parameters measured in the mutant cells directly with the wild-type data. In short, the Amira EM package (Pruggnaller *et al.*, 2008) was used to click points along the cytoplasmic leaflet of plasma membrane invaginations in a selected virtual slice of the electron tomogram that was positioned to contain the long axis of the invagination. The groups of points were transferred into a coordinate system such that the *x*-axis corresponded to the plasma membrane. A local second-degree polynomial was fitted through the points using MATLAB. This fit was used to measure the invagination length and radius of the invagination tip, as well as the appearance and position of a neck. The Amira EM package was also used to click points along the cytoplasmic leaflet of the vesicle membrane. This was done in the set of virtual slices that composed the whole vesicle, allowing us to fit an ellipsoid through the set of

points. From the major axes of the ellipsoid, we calculated the vesicle surface area. In tomograms that contained vesicles, we also clicked points on the plasma membrane throughout the tomographic volume. We then fitted a sphere through these points and determined the shortest distance from the vesicle center to the plasma membrane. To quantify the sizes of ribosome exclusion zones, we first generated an average of 11 consecutive virtual slices of which the central slice contained the invagination or the vesicle center. We overlaid this average with a hexagonal mesh of 50 nm spacing and determined which hexagons did not contain ribosomes, as well as which hexagons contained the plasma membrane. These data provided us with estimates for the diameter of the exclusion zone (parallel to the plasma membrane) as well as the height of the exclusion zone. To calculate the volume of the exclusion zones of invaginations, we assumed the shape of a half-ellipsoid with two equal short axes.

Statistics

For statistical analysis of the membrane shapes and exclusion zones, we used GraphPad Prism or R (https://cran.r-project.org/). All mutant data were compared with wild-type data (Kukulski *et al.*, 2012a). For the data that are normally distributed, we used an unpaired two-tailed Welch's test. To compare the exclusion zone volumes, the vesicle surfaces and their distance from the plasma membrane, we used a Mann–Whitney unpaired nonparametric test.

All measurements from CLEM data shown in the figures are listed in Supplemental File 4. Numbers (*n*) referring to CLEM data set sizes are technical replicates.

Endocytic sites with multiple invaginations or vesicles

As described for wild-type cells, in the correlative microscopy data set of mutant strains described here, we found endocytic sites that contained multiple endocytic events within the same exclusion zone (Kukulski *et al.*, 2012a). In the *sac6Δ* data set, one Sla1-GFP Abp1-mCherry spot contained two invaginations. These were included in all analysis.

In the *bbc1Δ* data set, of the 26 Rvs167-GFP/Abp1-mCherry spots, 6 contained multiple endocytic events. One site contained an invagination and a vesicle, one contained two invaginations, two contained two vesicles and two contained three vesicles each. Of 25 Sla1-GFP/Abp1-mCherry spots containing either invaginations or vesicles, four contained multiple events. One contained a vesicle and an invagination, two contained two invaginations, and one contained two vesicles. Of the 14 Abp1-mCherry spots in the absence of Sla1-GFP, two contained multiple events. One contained an invagination and a vesicle, and one contained three vesicles. We included these events in all analysis of membrane shape parameters. However, we did not use ribosome exclusion zones that contained multiple events for any quantification of exclusion zone sizes.

REFERENCES

Boldface names denote co–first authors

Aghamohammadzadeh S, Ayscough KR (2009). Differential requirements for actin during yeast and mammalian endocytosis. Nat Cell Biol 11, 1039–1042.

Basu R, Munteanu EL, Chang F (2014). Role of turgor pressure in endocytosis in fission yeast. Mol Biol Cell 25, 679–687.

Berro J, Pollard TD (2014). Synergies between Aip1p and capping protein subunits (Acp1p and Acp2p) in clathrin-mediated endocytosis and cell polarization in fission yeast. Mol Biol Cell 5, 295–303.

Berro J, Sirotkin V, Pollard TD (2010). Mathematical modeling of endocytic actin patch kinetics in fission yeast: disassembly requires release of actin filament fragments. Mol Biol Cell 21, 2905–2915.

Bieling P, Li TD, Weichsel J, Mcgorty R, Jreij P, Huang B, Fletcher DA, Mullins RD (2016). Force feedback controls motor activity and mechanical properties of self-assembling branched actin networks. Cell 164, 115–127.

Blanchoin L, Boujemaa-Paterski R, Sykes C, Plastino J (2014). Actin dynamics, architecture, and mechanics in cell motility. Physiol Rev 94, 235–263.

Boettner DR, Chi RJ, Lemmon SK (2011a). Lessons from yeast for clathrin-mediated endocytosis. Nat Cell Biol 14, 2–10.

Boettner DR, Friesen H, Andrews B, Lemmon SK (2011b). Clathrin light chain directs endocytosis by influencing the binding of the yeast Hip1R homologue, Sla2, to F-actin. Mol Biol Cell 22, 3699–3714.

Boucrot E, Pick A, Camdere G, Liska N, Evergren E, Mcmahon HT, Kozlov MM (2012). Membrane fission is promoted by insertion of amphipathic helices and is restricted by crescent BAR domains. Cell 149, 124–136.

Boulant S, Kural C, Zeeh J-C, Ubelmann F, Kirchhausen T (2011). Actin dynamics counteract membrane tension during clathrin-mediated endocytosis. Nat Cell Biol 13, 1124–1131.

Busch DJ, Houser JR, Hayden CC, Sherman MB, Lafer EM, Stachowiak JC (2015). Intrinsically disordered proteins drive membrane curvature. Nat Commun 6, 7875.

Campellone KG, Welch MD (2010). A nucleator arms race: cellular control of actin assembly. Nat Rev Mol Cell Biol 11, 237–251.

Chen Q, Pollard TD (2013). Actin filament severing by cofilin dismantles actin patches and produces mother filaments for new patches. Curr Biol 23, 1154–1162.

Collins A, Warrington A, Taylor KA, Svitkina T (2011). Structural organization of the actin cytoskeleton at sites of clathrin-mediated endocytosis. Curr Biol 21, 1167–1175.

Derenyi I, Julicher F, Prost J (2002). Formation and interaction of membrane tubes. Phys Rev Lett 88, 238101.

Dmitrieff S, Nedelec F (2015). Membrane mechanics of endocytosis in cells with turgor. PLoS Comput Biol 11, e1004538.

Galletta BJ, Cooper JA (2009). Actin and endocytosis: mechanisms and phylogeny. Curr Opin Cell Biol 21, 20–27.

Galletta BJ, Mooren OL, Cooper JA (2010). Actin dynamics and endocytosis in yeast and mammals. Curr Opin Biotechnol 21, 604–610.

Gardel ML, Shin JH, Mackintosh FC, Mahadevan L, Matsudaira P, Weitz DA (2004). Elastic behavior of cross-linked and bundled actin networks. Science 304, 1301–1305.

Gheorghe DM, Aghamohammadzadeh S, Smaczynska-De R II, Allwood EG, Winder SJ, Ayscough KR (2008). Interactions between the yeast SM22 homologue Scp1 and actin demonstrate the importance of actin bundling in endocytosis. J Biol Chem 283, 15037–15046.

Idrissi FZ, Blasco A, Espinal A, Geli MI (2012). Ultrastructural dynamics of proteins involved in endocytic budding. Proc Natl Acad Sci USA 109, E2587–E2594.

Idrissi FZ, Geli MI (2014). Zooming in on the molecular mechanisms of endocytic budding by time-resolved electron microscopy. Cell Mol Life Sci 71, 641–657.

Idrissi FZ, Grötsch H, Fernandez-Golbano IM, Presciatto-Baschong C, Riezman H, Geli MI (2008). Distinct acto/myosin-1 structures associate with endocytic profiles at the plasma membrane. J Cell Biol 180, 1219–1232.

Janke C, Magiera MM, Rathfelder N, Taxis C, Reber S, Maekawa H, Moreno-Borchart A, Doenges G, Schwob E, Schiebel E, Knop M (2004). A versatile toolbox for PCR-based tagging of yeast genes: new fluorescent proteins, more markers and promoter substitution cassettes. Yeast 21, 947–962.

Joglekar AP, Bouck DC, Molk JN, Bloom KS, Salmon ED (2006). Molecular architecture of a kinetochore-microtubule attachment site. Nat Cell Biol 8, 581–585.

Kaksonen M, Sun Y, Drubin DG (2003). A pathway for association of receptors, adaptors, and actin during endocytic internalization. Cell 115, 475–487.

Kaksonen M, Toret CP, Drubin DG (2005). A modular design for the clathrin- and actin-mediated endocytosis machinery. Cell 123, 305–320.

Koster G, Cacciuto A, Derenyi I, Frenkel D, Dogterom M (2005). Force barriers for membrane tube formation. Phys Rev Lett 94, 068101.

Kremer JR, Mastronarde DN, Mcintosh JR (1996). Computer visualization of three-dimensional image data using IMOD. J Struct Biol 116, 71–76.

Kubler E, Riezman H (1993). Actin and fimbrin are required for the internalization step of endocytosis in yeast. EMBO J 12, 2855–2862.

Kukulski W, Picco A, Specht T, Briggs JA, Kaksonen M (2016). Clathrin modulates vesicle scission, but not invagination shape, in yeast endocytosis. Elife 5, e16036.

Kukulski W, Schorb M, Kaksonen M, Briggs JA (2012a). Plasma membrane reshaping during endocytosis is revealed by time-resolved electron tomography. Cell 150, 508–520.

Kukulski W, Schorb M, Welsch S, Picco A, Kaksonen M, Briggs JA (2011). Correlated fluorescence and 3D electron microscopy with high sensitivity and spatial precision. J Cell Biol 192, 111–119.

Kukulski W, Schorb M, Welsch S, Picco A, Kaksonen M, Briggs JA (2012b). Precise, correlated fluorescence microscopy and electron tomography of lowicryl sections using fluorescent fiducial markers. Methods Cell Biol 111, 235–257.

Lawrimore J, Bloom KS, Salmon ED (2011). Point centromeres contain more than a single centromere-specific Cse4 (CENP-A) nucleosome. J Cell Biol, 195, 573–582.

Ma R, Berro J (2017). Structural organization and energy storage in cross-linked actin-assemblies. BioRxiv, https://doi.org/10.1101/237412.

Mastronarde DN (2005). Automated electron microscope tomography using robust prediction of specimen movements. J Struct Biol 152, 36–51.

McDonald K (2007). Cryopreparation methods for electron microscopy of selected model systems. Methods Cell Biol 79, 23–56.

Merrifield CJ, Feldman ME, Wan L, Almers W (2002). Imaging actin and dynamin recruitment during invagination of single clathrin-coated pits. Nat Cell Biol 4, 691–698.

Moreau V, Galan JM, Devilliers G, Haguenauer-Tsapis R, Winsor B (1997). The yeast actin-related protein Arp2p is required for the internalization step of endocytosis. Mol Biol Cell 8, 1361–1375.

Pelkmans L, Puntener D, Helenius A (2002). Local actin polymerization and dynamin recruitment in SV40-induced internalization of caveolae. Science 296, 535–539.

Picco A, Kaksonen M (2017). Precise tracking of the dynamics of multiple proteins in endocytic events. Methods Cell Biol 139, 51–68.

Picco A, Mund M, Ries J, Nédélec F, Kaksonen M (2015). Visualizing the functional architecture of the endocytic machinery. Elife 4, e04535.

Pollard TD (2007). Regulation of actin filament assembly by Arp2/3 complex and formins. Annu Rev Biophys Biomol Struct 36, 451–477.

Pollard TD, Borisy GG (2003). Cellular motility driven by assembly and disassembly of actin filaments. Cell 112, 453–465.

Powers TR, Huber G, Goldstein RE (2002). Fluid-membrane tethers: minimal surfaces and elastic boundary layers. Phys Rev E Stat Nonlin Soft Matter Phys 65, 041901.

Pruggnaller S, Mayr M, Frangakis AS (2008). A visualization and segmentation toolbox for electron microscopy. J Struct Biol 164, 161–165.

Rodal AA, Manning AL, Goode BL, Drubin DG (2003). Negative regulation of yeast WASp by two SH3 domain-containing proteins. Curr Biol 13, 1000–1008.

Rotty JD, Wu C, Bear JE (2013). New insights into the regulation and cellular functions of the ARP2/3 complex. Nat Rev Mol Cell Biol 14, 7–12.

Sato M, Schwarz WH, Pollard TD (1987). Dependence of the mechanical properties of actin/alpha-actinin gels on deformation rate. Nature 325, 828–830.

Sbalzarini IF, Koumoutsakos P (2005). Feature point tracking and trajectory analysis for video imaging in cell biology. J Struct Biol 151, 182–195.

Sirotkin V, Berro J, Macmillan K, Zhao L, Pollard TD (2010). Quantitative analysis of the mechanism of endocytic actin patch assembly and disassembly in fission yeast. Mol Biol Cell 21, 2894–2904.

Skau CT, Courson DS, Bestul AJ, Winkelman JD, Rock RS, Sirotkin V, Kovar DR (2011). Actin filament bundling by fimbrin is important for endocytosis, cytokinesis, and polarization in fission yeast. J Biol Chem 286, 26964–26977.

Skruzny M, Brach T, Ciuffa R, Rybina S, Wachsmuth M, Kaksonen M (2012). Molecular basis for coupling the plasma membrane to the actin

cytoskeleton during clathrin-mediated endocytosis. Proc Natl Acad Sci USA 109, E2533–E2542.

Skruzny M, Desfosses A, Prinz S, Dodonova SO, Gieras A, Uetrecht C, Jakobi AJ, Abella M, Hagen WJ, Schulz J, *et al* (2015). An organized co-assembly of clathrin adaptors is essential for endocytosis. Dev Cell 33, 150–162.

Stachowiak JC, Schmid EM, Ryan CJ, Ann HS, Sasaki DY, Sherman MB, Geissler PL, Fletcher DA, Hayden CC (2012). Membrane bending by protein-protein crowding. Nat Cell Biol 14, 944–949.

Sun Y, Kaksonen M, Madden DT, Schekman R, Drubin DG (2005). Interaction of Sla2p's ANTH domain with PtdIns(4,5)P2 is important for actin-dependent endocytic internalization. Mol Biol Cell 16, 717–730.

Sun Y, Martin AC, Drubin DG (2006). Endocytic internalization in budding yeast requires coordinated actin nucleation and myosin motor activity. Dev Cell 11, 33–46.

Suresh HG, Da Silveira Dos Santos AX, Kukulski W, Tyedmers J, Riezman H, Bukau B, Mogk A (2015). Prolonged starvation drives reversible sequestration of lipid biosynthetic enzymes and organelle reorganization in *Saccharomyces cerevisiae*. Mol Biol Cell 26, 1601–1615.

Svitkina TM (2013). Ultrastructure of protrusive actin filament arrays. Curr Opin Cell Biol 25, 574–581.

Taunton J, Rowning BA, Coughlin ML, Wu M, Moon RT, Mitchison TJ, Larabell CA (2000). Actin-dependent propulsion of endosomes and lyso-somes by recruitment of N-WASP. J Cell Biol 148, 519–530.

Wachsstock DH, Schwarz WH, Pollard TD (1994). Cross-linker dynamics determine the mechanical properties of actin gels. Biophys J 66, 801–809.

Welch MD, Way M (2013). Arp2/3-mediated actin-based motility: a tail of pathogen abuse. Cell Host Microbe 14, 242–255.

Winter D, Lechler T, Li R (1999). Activation of the yeast Arp2/3 complex by Bee1p, a WASP-family protein. Curr Biol 9, 501–504.